

1 **Past and Future Climate Variability Uncertainties in the Global Carbon Budget**
2 **using the MPI Grand Ensemble**

3 **T. F. Loughran¹, L. Boysen³, A. Bastos^{1,2}, K. Hartung^{1,*}, F. Havermann¹, H. Li³, J. E. M. S.**
4 **Nabel³, W. A. Obermeier¹, and J. Pongratz^{1,3}**

5 ¹Dept. of Geography, Ludwig Maximilian University, Munich, Germany.

6 ²Max Planck Institute for Biogeochemistry, Department of Biogeochemical Integration, Jena,
7 Germany.

8 ³Max Planck Institute for Meteorology, Hamburg, Germany.

9 ^{*}Now at: Deutsches Zentrum für Luft- und Raumfahrt, Institut für Physik der Atmosphäre,
10 Oberpfaffenhofen, Germany.

11 Corresponding author: Tamas Loughran (t.loughran@lmu.de)

12 **Key Points:**

- 13 • We use a single-model large ensemble to estimate uncertainties from internal climate
14 variability in the global carbon budget.
- 15 • The land sink accounts for most internal climate uncertainty which may permit 9–18
16 PgCyr⁻¹ in allowable emissions by 2050 (for 3°C warming).

17 Abstract

18 Quantifying the anthropogenic fluxes of CO₂ is important to understand the evolution of carbon
19 sink capacities, on which the required strength of our mitigation efforts directly depends. For the
20 historical period, the global carbon budget (GCB) can be compiled from observations and model
21 simulations as is done annually in the Global Carbon Project's (GCP) carbon budgets. However,
22 the historical budget only considers a single realization of the Earth system and cannot account
23 for internal climate variability. Understanding the distribution of internal climate variability is
24 critical for predicting the future carbon budget terms and uncertainties. We present here a
25 decomposition of the GCB for the historical period and the RCP4.5 scenario using single model
26 large ensemble simulations from the Max Planck Institute Grand Ensemble (MPI-GE) to capture
27 internal variability. We calculate uncertainty ranges for the natural sinks and anthropogenic
28 emissions that arise from internal climate variability, and by using this distribution, we
29 investigate the likelihood of historical fluxes with respect to plausible climate states. Our results
30 show these likelihoods have substantial fluctuations due to internal variability, which are
31 partially related to ENSO. We find that the largest internal variability in the MPI-GE stems from
32 the natural land sink and its increasing carbon stocks over time. The allowable fossil fuel
33 emissions consistent with 3°C warming may be between 9–18 PgCyr⁻¹. The MPI-GE is generally
34 consistent with GCP's global budgets with the notable exception of land-use change emissions in
35 recent decades, highlighting that human action is inconsistent with climate mitigation goals.

36 1 Introduction

37 The global carbon budget of CO₂ can be decomposed into anthropogenic emissions and natural
38 sinks. Anthropogenic emissions are mostly due to fossil fuel burning and fossil carbonates (E_{FF}),
39 but also from land-use induced land cover change and land management (“land-use change
40 emissions” in the following, E_{LUC}). The emitted CO₂ is then distributed into three natural sinks: it
41 is either assimilated by the land surface via ecosystem productivity (S_{LAND}), absorbed by the
42 ocean via diffusion and photosynthesis of marine organisms (S_{OCEAN}), or accumulated in the
43 atmosphere (atmospheric growth: G_{ATM}) leading to increased atmospheric CO₂ concentrations
44 (Le Quéré et al. 2013; Friedlingstein et al. 2020).

45 One of the key goals of the Global Carbon Project (GCP) is to evaluate anthropogenic
46 perturbations on the global carbon cycle and to understand the response of the natural carbon
47 sinks to increasing fossil emissions and land-use changes (e.g. Friedlingstein et al. 2020; Le
48 Quéré et al. 2018a,b). These global carbon budgets, conducted almost every year since 2007
49 (Canadell et al. 2008), provide an important understanding of the efficiency and potential
50 saturation of the natural sinks. This in turn is essential knowledge for predicting the future sink
51 capacities and, therefore, the required strength for future climate mitigation targets and of
52 “allowable” emissions under given climate targets. A comprehensive understanding of
53 uncertainties in these budgets is essential for guiding policy and decision-making.

54 The components of the GCP carbon budgets are associated with large uncertainties,
55 which are based on a combination of observation and model uncertainties. Fossil emissions are
56 based on energy and fuel consumption data whereby the uncertainties lie in the fuel
57 consumption, fuel carbon content, and combustion efficiency (Andres et al. 2012). The E_{LUC}
58 estimate is based on three bookkeeping models, in which estimates of land-use transitions are
59 combined with observation-based carbon densities to track terrestrial emissions and removals

60 according to empirical temporal response curves for each ecosystem (Hansis et al. 2015;
61 Houghton and Nassikas 2017). The corresponding estimates for E_{LUC} uncertainty have low
62 confidence and are based on expert knowledge, which considers the bookkeeping models and the
63 range of the 17 global dynamical vegetation models (DGVMs) (Friedlingstein et al. 2020). The
64 ocean sink estimate is based on the standard deviation of nine global ocean biogeochemical
65 models and their consistency with observed CO_2 partial pressure-based flux estimates. The
66 terrestrial sink in earlier budgets was estimated as a residual from all other terms or based on
67 DGVMs from the 2019 budget onwards. The estimates of both S_{LAND} and S_{OCEAN} are evaluated to
68 have medium confidence (Friedlingstein et al. 2020). When estimating the land sink with
69 DGVMs, the G_{ATM} cannot be matched, leading to a “budget imbalance” term of $\sim 0.4 \text{ Pg C yr}^{-1}$.
70 While atmospheric measurements of CO_2 concentration are relatively more accurate, there are
71 substantial interannual variations (IAV) driven by natural climate variability (Dlugokencky and
72 Tans 2018; Conway et al. 1994).

73 From such global carbon budgets, it is possible to quantify the future emissions to stay
74 within a given trajectory of climate change (Rogelj et al. 2016, Millar et al. 2016). However,
75 estimating these “allowable emissions” from historical budgets actually requires considering an
76 additional source of uncertainty: the internal variability of the climate system. The uncertainties
77 in the GCP budgets are related to observational and model uncertainties while uncertainties
78 associated with internal climate variability are not directly addressed.

79 Much of the IAV in CO_2 concentration and its impacts on the regional (Zhu et al. 2018)
80 and global carbon sinks (Bastos et al. 2013, Ballantyne et al. 2012) is driven by internal
81 variability in the climate system. Internal variability arises from stochastic processes and
82 feedbacks in the coupled ocean-atmosphere system (e.g. El Niño–Southern Oscillation; ENSO)
83 and is difficult to predict due to high sensitivity to initial conditions and the chaotic evolution of
84 the Earth system (Deser et al. 2012). Traditionally, internal variability in weather and climate
85 forecasts is accounted for by performing ensemble forecasting, i.e. running multiple simulations
86 of the same (or several) models started from perturbed initial conditions, in order to estimate the
87 distribution of future climate states (Deser et al. 2012).

88 The importance of considering the full range of potential climate states due to internal
89 climate variability is particularly pertinent to future estimates of the carbon budget, where the
90 exact climate state (and consequently the strength of the natural sinks) in a given year is
91 unknown. Using only one realization may not robustly capture these future states. Furthermore,
92 we cannot assume that the variance of the natural CO_2 fluxes is stationary under increasing
93 atmospheric CO_2 . It is not possible to estimate the range of plausible carbon budget fluxes due to
94 internal climate variability using only one instance of historical observations or observationally
95 forced model simulations. Using ensemble simulations will allow for a more robust calculation
96 of future trends in the mean and variability of the carbon budget terms (e.g. Kay et al. 2015).

97 Since the historical observation-based carbon budget uncertainty only considers one
98 realization of internal climate variability, the influence of internal climate variability on each
99 budget term is unknown. Therefore, we ask the following research questions:

- 100 • How large is the uncertainty from internal climate variability in the global carbon budget
101 terms and how does it compare to the variability of the latest global carbon budget
102 (GCB2020) values?

- 103 • How likely were the historical carbon fluxes with respect to the distribution of possible
 104 fluxes from internal climate variability and what drove those anomalies?
- 105 • How will the carbon budget components and their internal variability change in the future
 106 (e.g. under RCP4.5)?

107 In this study, we estimate uncertainties associated with internal climate variability for
 108 each component of the carbon budget using a large ensemble of single-model simulations from
 109 the Max Planck Institute Grand Ensemble project (MPI-GE; Maher et al. 2019). We compare the
 110 results of the estimates for internal climate variability uncertainties to the uncertainties of the
 111 recent GCB2020 (Friedlingstein et al. 2020). Furthermore, we discuss the suitability and possible
 112 limitations of using a large ensemble of simulations for better understanding variability and
 113 uncertainties associated with E_{LUC} and S_{LAND} and how many ensemble members are required to
 114 answer these questions.

115 2 Methods

116 2.1 Overview of models and simulations

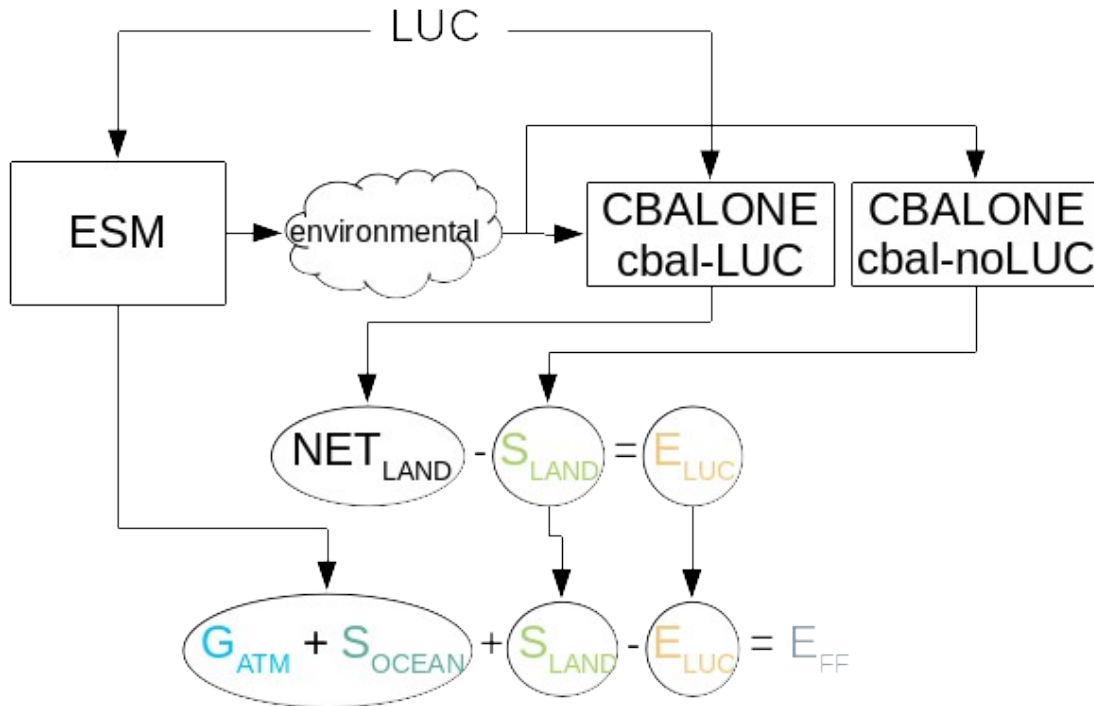
117 The methods used to generate the ensemble of climate realizations as part of the MPI-GE project
 118 are fully described in Maher et al. (2019). Therefore, we only give a summary here. The MPI-GE
 119 is a single model large ensemble project that uses the Max Planck Institute Earth System Model
 120 (MPI-ESM; for a full description see Giorgetta et al. 2013) version 1.1. The MPI-ESM is
 121 composed of an atmospheric component provided by ECHAM 6.3.01p3 (Stevens et al. 2013) run
 122 at T63L47 resolution ($\sim 1.8^\circ$ and 47 vertical layers), an ocean component provided by MPIOM
 123 1.6.1p1 (Marsland et al. 2003) run at GR15L40 resolution ($\sim 1.5^\circ$), the ocean biogeochemistry
 124 model HAMOCC5.2 (Ilyina et al. 2013), and the land component JSBACH3 (Reick et al. 2013,
 125 Goll et al. 2015). 100 ensemble members are generated by branched initialization (every ~ 6 –24
 126 years) from a sub-sample of years from a pre-industrial control (piControl) simulation. The
 127 piControl as well as the subsequent historical and future simulations follow the protocol of
 128 concentration-driven Earth system model runs of the Coupled Model Intercomparison projects
 129 (CMIP), in this case specifically CMIP5 (Taylor et al. 2012).

130 The JSBACH3 component simulates transitions in land cover types with respect to both
 131 natural vegetation dynamics and land-use changes. However, we utilize a smaller standalone
 132 sub-component of JSBACH3 called Carbon Balance ALONE (CBALONE) to differentiate the
 133 emissions due to land-use change from the remaining net land sink (as is done in e.g. Roeckner
 134 et al. 2010). *As in all Earth system model simulations that perform historical or scenario
 135 simulations, anthropogenic and natural effects occur concurrently, i.e. the simulations only
 136 provide the net land-atmosphere exchange (i.e. $S_{LAND} + E_{LUC}$). Only instantaneous emissions to
 137 the atmosphere can be derived directly from the historical or scenario simulations (as, e.g., in
 138 Lawrence et al. 2012). These, however, neglect legacy emissions that result in particular from the
 139 slow decay of wood products, harvested material left on site, and the adjustment of soil carbon
 140 stocks to the altered land-use over decades to centuries, but also comprise slow carbon uptake in
 141 processes like forest regrowth. In order to capture all fluxes from land-use change (instantaneous
 142 and legacy), additional simulations are essential that exclude the land-use change forcing, such
 143 that by difference to the historical or scenario simulation E_{LUC} can be isolated (Pongratz et al.,
 144 2014). Note that effects of altered atmospheric CO_2 concentrations by E_{LUC} , with emissions
 145 creating a compensating carbon sink in land and ocean (the “land-use feedback”), are excluded*

146 in our concentration-driven feedback (Pongratz et al. 2014). Similarly, since CBALONE is
147 driven with the climate from the coupled simulation, changes in surface climate due to land-use
148 change also act the same way in both simulations. Thus, the difference between the simulations
149 with (MPI-GE) and without land-use change (CBALONE) cancels these effects (apart from
150 secondary-order terms) and excludes resulting feedbacks. This is essential to make our estimates
151 consistent with the methodology used in the GCB2020 for the terrestrial budget terms.

152 CBALONE includes only the long-term dynamics associated with carbon turnover rates
153 and vegetation biogeography. We force CBALONE with daily data from 100 climate realizations
154 taken from the MPI-GE, both with and without anthropogenic land-use change (LUC and
155 noLUC simulations respectively) comparable to the approach taken by the GCP (Friedlingstein
156 et al. 2020). The land-use change transition data utilized by MPI-GE and CBALONE are taken
157 from the Land Use Harmonization 2 project (LUH2; Hurtt et al. 2011). While the carbon fluxes
158 from CBALONE did not exactly match JSBACH3 estimates, they consistently simulate
159 JSBACH3 fluxes to within 5% accuracy (Figure S6). Therefore, the CBALONE simulations with
160 land-use change are required so that E_{LUC} could be calculated independent of the small
161 CBALONE error (in absence of the error, the net land-atmosphere exchange could have been
162 directly provided by the MPI-GE simulations).

163 The climate realizations used to force CBALONE were taken from existing daily output
164 from the MIP-GE historical and RCP4.5 scenarios (1850–2099; Table 1). We chose the RCP4.5
165 scenario as a scenario of medium climate change that estimates the CO₂ emissions under climate
166 policies designed to limit global warming to no more than 3°C over present-day temperatures,
167 allowing us to create uncertainty estimates of fossil emissions that are consistent with this goal.
168 The daily model output variables that are used to force CBALONE include 2m air temperature,
169 soil temperature, precipitation, net primary productivity (NPP) per plant functional type (PFT),
170 leaf area index (also per PFT), and maximum wind. These variables are marked as
171 “environmental” in Figure 1.



172

173 **Figure 1.** Workflow schematic for simulations and carbon budget decomposition for each
 174 ensemble member. Variables from MPI-GE labeled “*environmental*” include leaf area index, net
 175 primary productivity, topsoil temperature, maximum 10m wind speed, air temperature and
 176 precipitation (see section 2.2).

177

178

179 **Table 1.** Experiment simulations. Each experiment has 100 ensemble members. The MPI-GE
 180 simulations have been labeled with the prefix “mpige”, while the CBALONE simulations are
 181 labeled as “cbal”. The scenarios are labeled with the suffix “hist” for the historical scenario and
 182 “rcp4.5” for the future scenario. Both scenarios for CBALONE are simulated with land-use
 183 change (labeled with LUC) and without land-use change using 1850 land-use throughout the
 184 simulation (labeled with noLUC). There are only 97 ensemble members for the CBALONE
 185 RCP4.5 scenario because a few MPI-GE output files required by CBALONE contained
 186 erroneous data.

	LUC	No LUC
Historical (1850–2005)	mpige-LUC-hist cbal-LUC-hist	cbal-noLUC-hist
RCP 4.5 (2006–2099)	mpige-LUC-rcp4.5 cbal-LUC-rcp4.5	cbal-noLUC-rcp4.5

187

188 2.2 Carbon budget decomposition

189 The carbon budget is decomposed here into various source and sink terms as in Friedlingstein et
 190 al. (2019), utilizing output from the MPI-GE and the CBALONE simulations. The monthly
 191 CBALONE output is aggregated to annual values for comparison to the GCB2020. The cbal-
 192 noLUC simulation provides land-atmosphere exchange that would occur without land-use
 193 changes, and thus S_{LAND} is calculated as the net biome productivity (NBP) from this simulation.
 194 Equation 1 clarifies components of NBP taken from the model, where NPP is net primary
 195 productivity, RH is heterotrophic respiration, fFire is carbon flux due to wildfires, fHarvest is
 196 carbon flux due to crop and wood harvest, fGrazing is carbon flux due to herbivorous grazing,
 197 and fLCC is the instantaneous emissions from land-use induced land cover changes. The fLCC
 198 term is zero in the cbal-noLUC simulations.

$$NBP = S_{LAND} = NPP + RH + fFire + fHarvest + fGrazing + fLCC \quad (1)$$

199

200 E_{LUC} is calculated as the difference in NBP between the cbal-LUC and cbal-noLUC
 201 simulations (Equation 2; note that fluxes to the natural sinks are negative values and fluxes to the
 202 atmosphere are positive consistent with Friedlingstein et al. 2020). Correspondingly, the NBP
 203 from the cbal-LUC simulation is equivalent to the net land-atmosphere exchange (NET_{LAND}).

$$E_{LUC} = NBP|_{cbal-LUC} - NBP|_{cbal-noLUC} = NET_{LAND} - S_{LAND} \quad (2)$$

204

205 G_{ATM} and S_{OCEAN} are taken directly from the MPI-GE output. The implied “compatible”
 206 emissions (also E_{FF}) are calculated as the residual of all other terms in the budget (Equation 3 &
 207 Figure 1), as described in Roeckner et al. (2010) and Jones et al. (2013). These are the emissions
 208 that would need to occur for CO_2 to be conserved given particular atmospheric concentration,
 209 land-use emissions, and natural sink fluxes. This is different from the GCB2020 approach, where
 210 all terms were determined independently based on model or observational estimates, which
 211 requires a budget imbalance term to be added.

$$E_{FF} + E_{LUC} = G_{ATM} + S_{OCEAN} + S_{LAND} \quad (3)$$

212

213 We calculated the full decomposition of the carbon budget for each ensemble member of
 214 the historical and RCP4.5 scenarios and compare it to the GCB2020 (Friedlingstein et al. 2020)
 215 as the best estimate of the real global carbon cycle. Decadal averages of the MPI-GE ensemble
 216 mean and standard deviation are calculated for a direct comparison with the decadal mean and
 217 uncertainties presented in the GCB2020. To assess the magnitude of the uncertainties due to
 218 internal climate variability compared to the magnitude of the budget terms, we further calculate
 219 the signal-to-noise ratio (SNR) of each term as the ensemble mean divided by the ensemble
 220 standard deviation.

221 2.3 Interannual variability

222 While internal climate variability may contribute to interannual variations in carbon fluxes to the
 223 natural sinks, there are also variations driven by non-internal climate related factors, for example
 224 changes in anthropogenic activity ($E_{FF} + E_{LUC}$) and volcanism. An assessment of uncertainties
 225 based on temporal standard deviations would be a mixture of internal and non-internal

226 variability, while an ensemble standard deviation at a given time step would reflect variations
 227 only due to internal climate variability. In order to assess future uncertainties, it is important that
 228 the model can simulate historical IAV appropriately. Here we assess the ability of individual
 229 MPI-GE and CBALONE ensemble members to adequately represent the temporal standard
 230 deviation of the historical year-to-year climate variations in each GCB2020 budget term.
 231 Therefore, we define a reference IAV as the temporal standard deviation of annual fluxes over
 232 the base period 1961–1990 (World Meteorological Organization standard reference period). All
 233 models have unique imperfections in their ability to simulate the statistical properties of the
 234 carbon fluxes such as mean and standard deviation, which we refer to as model bias.
 235 Furthermore, each may have a different trend over the base period which would artificially alter
 236 the IAV. To remove the model biases in the ensemble mean of the MPI-GE, we detrend the
 237 budget terms of each ensemble member before calculating IAV using an ordinary least-squares
 238 regression (OLR) of the ensemble mean over the historical period 1959–2005. We also detrended
 239 each model used in the GCB2020 and calculate the IAV over the same period.

240 2.4 Probability of exceedance of past budget terms

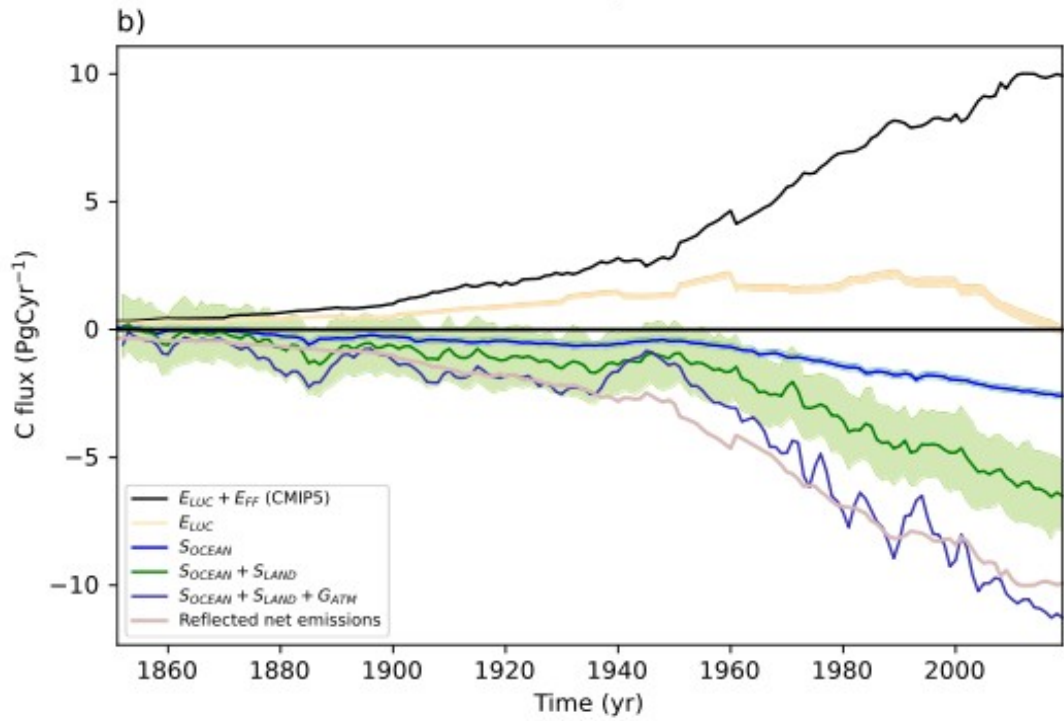
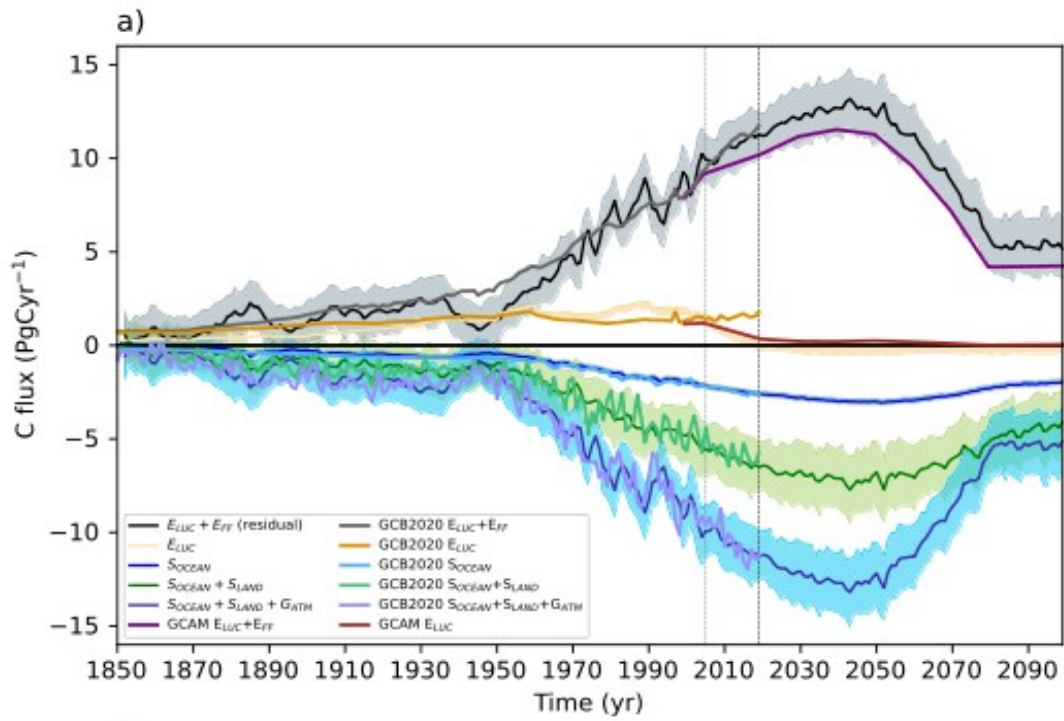
241 To evaluate how likely past carbon fluxes were compared to the range of possible climate states
 242 due to internal variability, we describe here a measure of the probability of exceedance.
 243 Supposing a relatively small amount of CO₂ uptake by the land surface in a particular year, it is
 244 quite likely that under more favorable climate conditions for carbon storage this land CO₂ uptake
 245 would be exceeded. Therefore, we aim to calculate the probability that the MPI-GE members are
 246 greater than the GCB2020 multi-model mean (which we assume to be the closest estimate to
 247 historical CO₂ fluxes). Each budget term for the MPI-GE and GCB2020 is OLR detrended in the
 248 same way as described above (Section 2.3) except that we use the 1959–2018 period (i.e. the
 249 longest available common period for GCB2020 and the MPI-GE simulations). For each year and
 250 budget term, we calculate the corresponding cumulative distribution functions (“exceedance”) of
 251 the MPI-GE ensemble members using a kernel density estimator (Scott 2015). We then evaluate
 252 the GCB2020 terms on the complement of the cumulative distribution functions (1 – Pr.) to find
 253 their occurrence probability (e.g. see Figure S3). Since we use a cumulative distribution, the
 254 complement probability is the “exceedance probability” of the ensemble spread being larger than
 255 the historical value. Unusually large historical fluxes will therefore have low probability of
 256 exceedance. This is similar to the probability of exceedance calculations from studies on climate
 257 extremes (e.g. Suarez-Gutierrez et al. 2020).

258 Finally, we assess the relationship of the GCB2020 exceedance probabilities for S_{LAND}
 259 and S_{OCEAN} fluxes to ENSO, since this is the most prominent mode that drives internal climate
 260 variability (Dannenberget al. 2015; Zhang et al. 2019). We use the annual mean Niño 3.4 index
 261 from the NOAA Climate Prediction Center (Climate Prediction Center 2017) which uses ERSST
 262 V5 (Huang et al. 2017) sea surface temperatures averaged over the region 5°N–5°S, 170–120°W.
 263 We then calculate the Pearson’s correlation coefficient and the OLR between the exceedance
 264 probabilities of the natural sinks and the Niño 3.4 index. We test the significance of this
 265 correlation using a two-sided t-test under the null hypothesis that a relationship between the
 266 exceedance probabilities of the GCB2020 fluxes and ENSO state can be rejected at the 95%
 267 confidence level. Since these methods assume normally distributed data, we beforehand tested
 268 the normality of the budget terms and their probabilities using the Shapiro-Wilk test for
 269 normality (Shapiro and Wilk, 1965). We found that all budget terms (except for G_{ATM}) are
 270 normally distributed in the 1850–2018 period.

271 3 Results**272 3.1 Temporal evolution of budget components and internal climate variability**
273 uncertainties

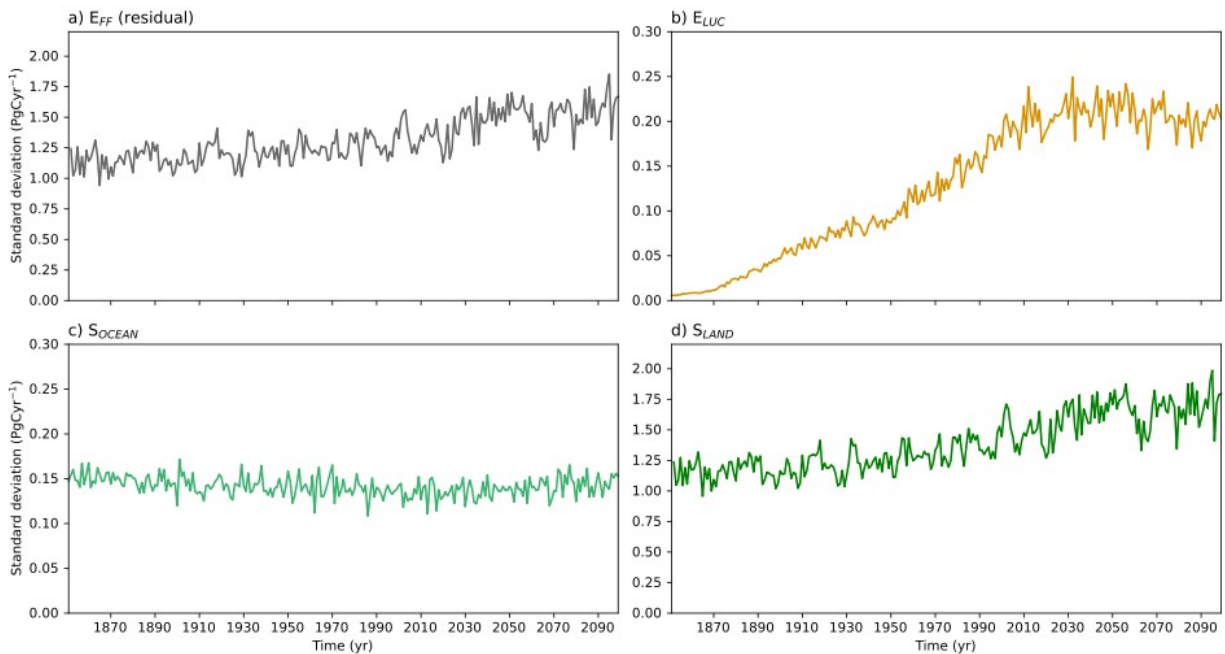
274 The historical period and RCP4.5 scenario have globally increasing CO₂ fluxes from the
275 atmosphere to the land and ocean sinks until about 2040 before decreasing thereafter (see Figure
276 2) due to assumed RCP4.5 mitigation measures. The decrease in land and ocean sink is because
277 G_{ATM} in RCP4.5 decelerates after 2040 resulting in an atmospheric concentration of ~525 ppm
278 CO₂ by 2100 (Thomson et al. 2011). The compatible fossil emissions in the MPI-GE (E_{FF} in
279 Figure 2) share similar temporal evolution of the natural sinks. On the other hand, E_{LUC} is driven
280 by the LUH2 land-use data set and is independent of fossil emissions, which increases until
281 about 1990 before becoming a weak net sink from around 2020 onward under the RCP4.5
282 scenario (Figure 2 and S1 b). Within the period 1970–2010, the ensemble means of the G_{ATM} and
283 E_{FF} terms show annual to decadal-scale variations, which are a known feature of the CO₂
284 concentration forcing used in the historical period (caused by the introduction of additional CO₂
285 observation stations in the 1960s, see Figure 10 of Meinshausen et al. 2017) and are not
286 internally driven variations in the MPI-ESM. The S_{LAND} and S_{OCEAN} do not immediately respond
287 to such rapid changes in G_{ATM} since they are dominated by the climate state and its variability. It
288 then follows that these variations are evident in the residual E_{FF} term.

289



291 **Figure 2.** Stacked decomposition of the CO₂ budget terms from the MPI-GE for the historical
 292 (1850–2005) and RCP4.5 (2006–2099) scenarios (a) (unstacked plots of the individual terms can
 293 be found in Figure S1). Thick lines mark the ensemble mean and shading marks the range of the
 294 ensemble ± 1 standard deviation. Overlaid are the GCB2020 budget terms for comparison.
 295 Vertical lines mark the end of the historical period (2006) and the end of the latest GCP budget
 296 (2019). An alternative budget using the CMIP5 E_{FF} taken from Andres et al. (2012) is also
 297 provided (b). The pink line shows the reflected net emissions, the difference with the net natural
 298 sinks would give the simulated B_{IM} term in Figure S1 f.

299 The budget terms in Figure 2 are stacked for S_{LAND} and G_{ATM} , and hence the shown
 300 standard deviation of the ensemble members for these terms aggregates according to a normal
 301 sum distribution (i.e., $\sigma(S_{OCEAN}+S_{LAND})=\sqrt{[\sigma^2(S_{OCEAN}) + \sigma^2(S_{LAND})]}$). The atmospheric
 302 concentration is prescribed to be the same for all ensemble members, and so G_{ATM} has no
 303 ensemble standard deviation. The standard deviation of residual E_{FF} is inherited directly from the
 304 net natural sinks and E_{LUC} because it is calculated as a residual in the budget. S_{OCEAN} has a stable
 305 standard deviation of ~ 0.15 Pg C yr⁻¹ (Figure 3 c), which does not have a trend. S_{LAND} has the
 306 largest standard deviation throughout the historical period and the RCP4.5 scenario (see Figure 3
 307 d), therefore the standard deviation of the net of natural sinks in Figure 2 (and consequently
 308 residual E_{FF}) mostly originates from S_{LAND} . Standard deviation increases with time for residual
 309 E_{FF} and S_{LAND} (Figure 3 a & d) from ~ 1 Pg C yr⁻¹ in 1850 to ~ 1.5 Pg C yr⁻¹ in 2100. E_{LUC} standard
 310 deviation gradually increases from almost 0 to ~ 0.2 Pg C yr⁻¹ by 2010 and later (Figure 3 b).

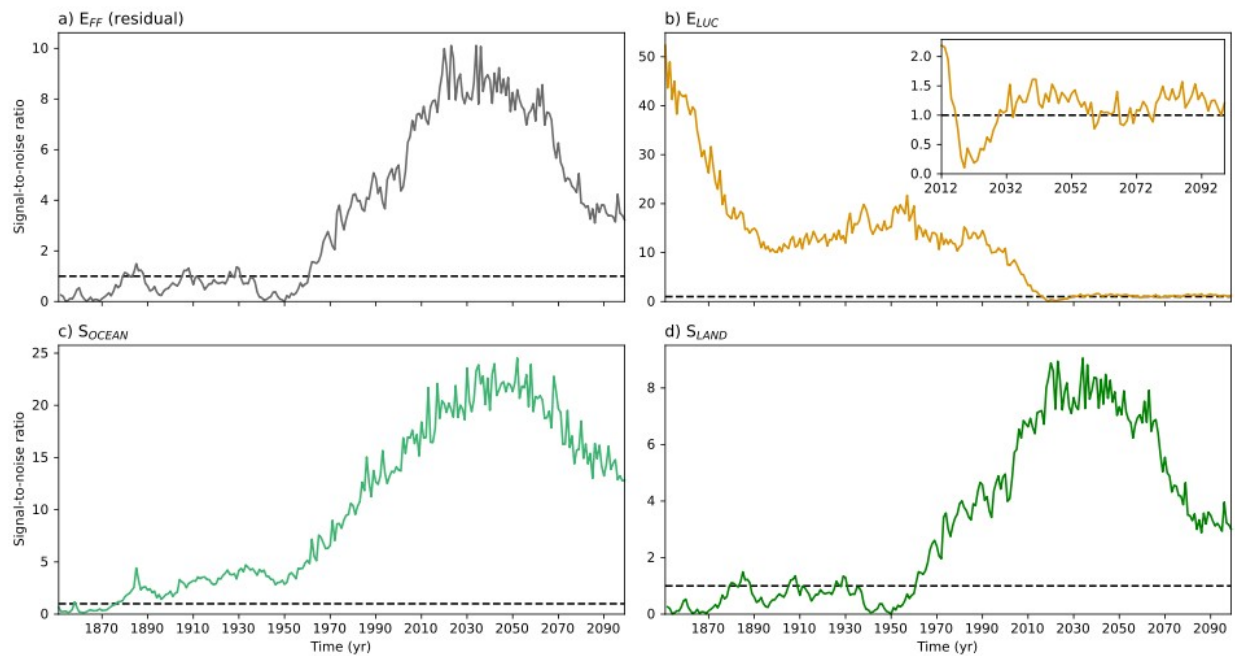


311

312 **Figure 3.** Yearly ensemble standard deviation for each carbon budget term. The emissions are on
 313 the top (a residual E_{FF} & b E_{LUC}) and the natural sink terms are on the bottom (c S_{OCEAN} & d
 314 S_{LAND}).

315 The importance of internal climate-driven variations (Figure 3) relative to the ensemble
 316 mean state can be better understood by analyzing the SNRs (Figure 4). Values greater than one
 317 indicate that the mean state dominates the signal, whereas values less than one indicate that the

318 internal climate variability uncertainty is the dominant factor in the carbon fluxes. For residual
 319 E_{FF} and S_{LAND} (Figure 4 a & d), internal variations are more relevant up until 1970. After that, the
 320 mean carbon fluxes (i.e. the forced signal) are much larger than the variations due to internal
 321 climate variability, for example ~ 2.5 – 3 times greater for S_{LAND} . S_{OCEAN} generally follows the same
 322 pattern (Figure 4 c); the internal climate variability remains several times smaller than the mean
 323 carbon flux to the ocean from about 1890 onward. On the other hand, the standard deviation in
 324 E_{LUC} is as large as the mean from 2010 onward (Figure 4 b), however, this is likely a
 325 consequence of the simulation setup: land-use changes begin in 1850 but the full range of
 326 variation from the legacy emissions of land-use change does not manifest until several decades
 327 later. This means the E_{LUC} SNR is effectively only valid under the future scenario when the mean
 328 E_{LUC} is small.



329

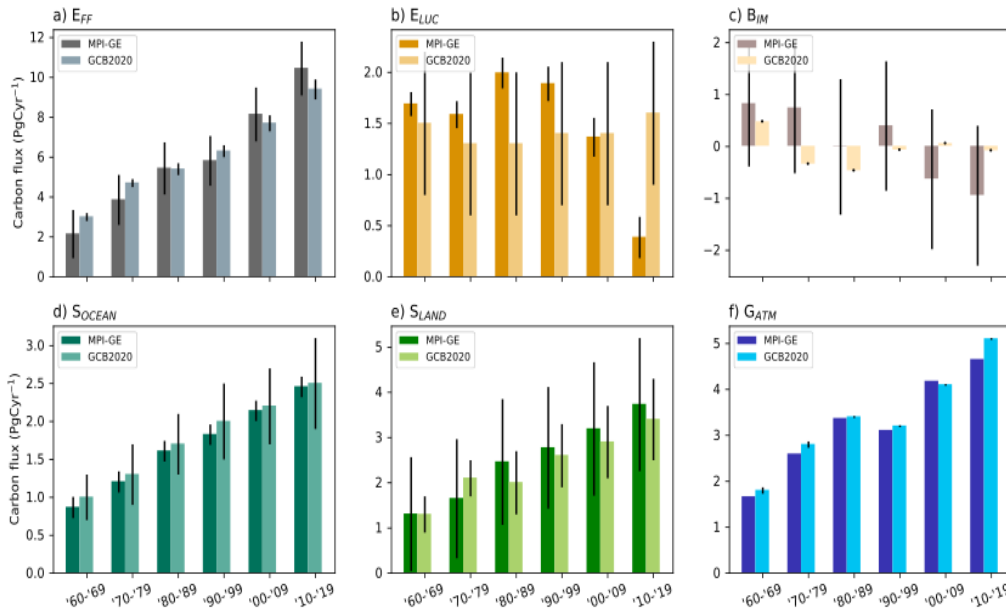
330 **Figure 4.** Yearly signal-to-noise ratio for each budget term in the MPI-GE. Dashed lines
 331 delineate ratio 1, where the standard deviation of the respective flux equals the mean flux. E_{LUC}
 332 has an inset plot with the post 2010 period zoomed in, when variations from legacy land-use
 333 fluxes have fully established.

334 3.2 Comparison to GCB2020

335 3.2.1 Comparison of means

336 We compare here the GCB2020 mean of each budget term to the ensemble mean of the MPI-GE
 337 for each decade, before comparing the variances in the following sections. Firstly, the residual
 338 E_{FF} mean increases faster in the MPI-GE than observed in the GCB2020 (Figure 5 a). Initially,
 339 MPI-GE residual E_{FF} in the 1960s is less than the GCB2020 estimate by 0.8 Pg C yr^{-1} while it is
 340 greater than it by 1.3 Pg C yr^{-1} in the 2010–2018 decade. However, the range of GCB2020 means
 341 is well within the range of values simulated by the MPI-GE. Secondly, there are large differences
 342 in the mean E_{LUC} fluxes between MPI-GE and GCB2020 (Figure 5 b). MPI-GE E_{LUC} is larger
 343 compared to GCB2020 in decades prior to 2000, however, these values are also within the large

344 uncertainty ranges of the GCB2020. In recent decades, the MPI-GE estimates lower E_{LUC} than
 345 the GCB2020. Thirdly, S_{LAND} tends to be slightly higher in the MPI-GE for almost all decades
 346 (Figure 5 e). Fourthly, S_{OCEAN} mean fluxes in MPI-GE and GCB2020 are very similar (Figure 5
 347 d). Lastly, G_{ATM} in MPI-GE has similar decadal variations as GCB2020, both displaying a dip in
 348 the 1990s, and there is no consistent bias (Figure 5 f).



349

350 **Figure 5.** Decadal average of carbon flux budget terms (bars), and the uncertainty expressed as
 351 ± 1 standard deviation from the mean (error whiskers). The MPI-GE uncertainties are ensemble
 352 standard deviations and the GCB2020 uncertainties are multi model standard deviations. The
 353 dark bars are the MPI-GE and the lighter bars are the GCB2020 values taken from Friedlingstein
 354 et al. (2019). The top row (a and b) are the emissions and the simulated budget imbalance term
 355 (c) as shown in Figure 2 b, and the bottom row (d, e and f) are the sink terms.

356 3.2.2 Un-bias-corrected comparison of uncertainties

357 The uncertainty ranges in Figure 5 are based on ensemble standard deviations for MPI-GE (and
 358 therefore reflect internal climate variability uncertainties) and multi-model standard deviation for
 359 GCB2020. These ranges can tell us two things: how realistic the MPI-GE range of fluxes is
 360 compared to observations, and how large uncertainties associated with internal climate
 361 variability are compared to other sources of uncertainty (e.g. from observational measurements
 362 or the differing process representations in the different GCB2020 models). Therefore, we will
 363 determine here whether the GCB2020 mean state lies outside the MPI-GE uncertainty ranges for
 364 each budget term.

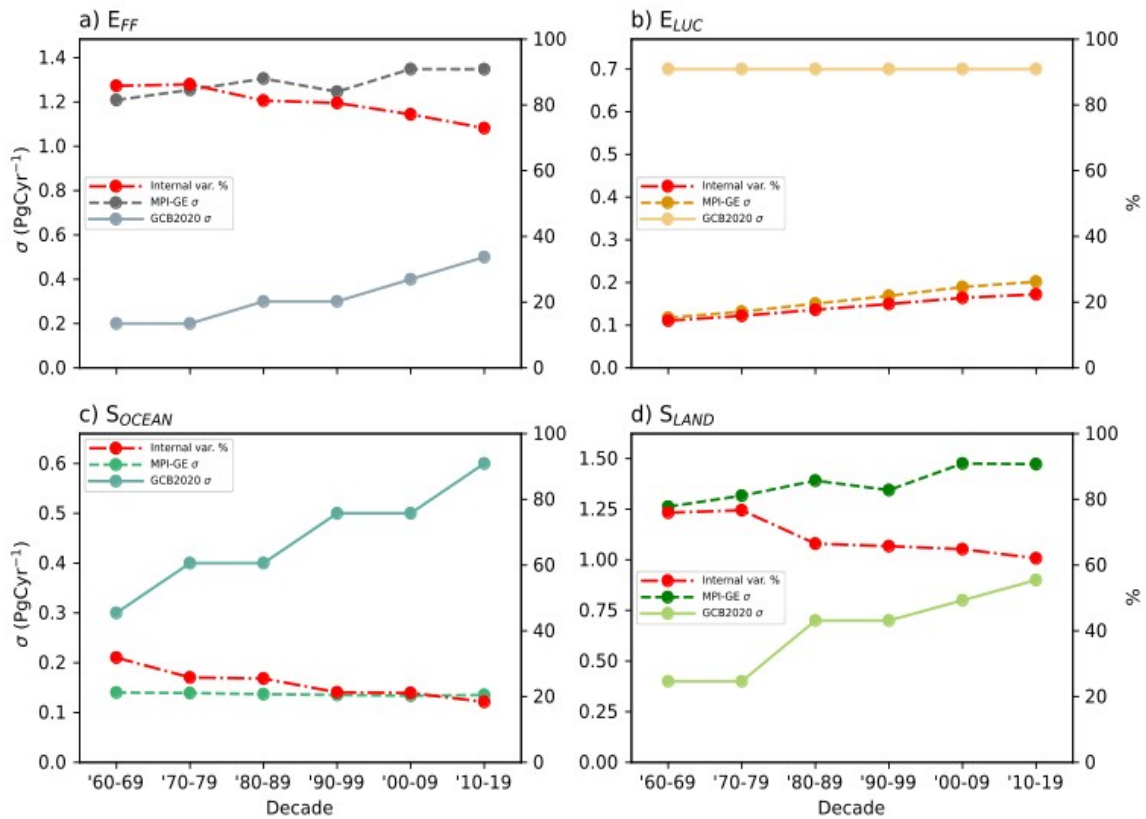
365 Residual E_{FF} , B_{IM} (based on the budget in Figure 2 b) and S_{LAND} (Figure 5 a, c & e) have
 366 larger standard deviations in the MPI-GE compared to GCB2020, i.e. internal variability is a
 367 larger source of error than observational and model uncertainty (more detail follows in 3.2.3).
 368 The GCB2020 mean for these budget terms falls within the uncertainty range due to internal
 369 climate variability, demonstrating the capability of MPI-GE to capture the observed carbon flux.

370 On the other hand, E_{LUC} and S_{OCEAN} have a narrower range of internal climate variability
 371 uncertainty in the MPI-GE compared to the modeled uncertainty in the GCB2020 (Figure 5 b &
 372 d). While the GCB2020 mean is within the MPI-GE uncertainty for S_{OCEAN} for most decades
 373 (indicating consistency between the two), E_{LUC} GCB2020 means are outside the corresponding
 374 MPI-GE ranges for nearly all decades. However, the uncertainty ranges of MPI-GE and
 375 GCB2020 overlap for both S_{OCEAN} and E_{LUC} , i.e. certain ensemble members match certain
 376 GCB2020 models. Only, the E_{LUC} 2009–2018 mean and standard deviation of the GCB2020 is
 377 outside the standard deviation range of uncertainty due to internal climate variability, indicating
 378 clear inconsistency (see discussion section 4.1).

379 There is no uncertainty range for G_{ATM} from MPI-GE (Figure 5 f) since all ensemble
 380 members are prescribed with the same atmospheric CO_2 concentration. The error whiskers in the
 381 G_{ATM} GCB2020 are derived from various observational uncertainties, which are very small
 382 compared to the terms that are simulated by dynamical models (S_{LAND} , S_{OCEAN} , and E_{LUC}).
 383 Because the MPI-GE CO_2 concentration starting 2006 is derived from the Global Change
 384 Assessment Model (GCAM; Thomson et al. 2011), the difference in G_{ATM} between MPI-GE and
 385 the GCB2020 for the last two decades may in part be due to the differences in carbon cycle
 386 processes that are represented in MPI-ESM and GCAM.

387 3.2.3 Bias-corrected comparison of uncertainties

388 To more directly evaluate the magnitude of the historical uncertainties associated with internal
 389 climate variability compared to the GCB2020, Figure 6 shows the standard deviations where the
 390 biases in the means have been removed (centered). The models used in the GCB2020 estimates
 391 are forced by only one realization of the climate state—the actual historical climate evolution.
 392 Therefore, the plausible carbon fluxes under different climate states cannot be inferred using
 393 only the GCB2020, and while the models used in the GCB2020 do contain internal climate
 394 variability, the multi-model standard deviations only account for model uncertainty, but not that
 395 from natural variability. If we assume that there is no or negligible uncertainty due to internal
 396 climate variability associated with the multi-model GCB2020 standard deviation and that the
 397 standard deviation of the MPI-GE is entirely due to internal climate variability, then we can find
 398 the proportion of the total uncertainty attributable to internal climate variability (i.e. the sum of
 399 GCB2020 and MPI-GE uncertainties; red lines in Figure 6). The importance of internal climate
 400 variability decreases with time for S_{LAND} and residual E_{FF} and the MPI-GE land sink uncertainty
 401 increases faster than the multi-model uncertainty in the GCB2020. For the 2009–2018 decade the
 402 contribution of internal climate variability to total uncertainty is 70% for the residual E_{FF} and
 403 60% for S_{LAND} . A constant multi-model uncertainty was assumed for E_{LUC} in the GCB2020 and
 404 therefore the MPI-GE E_{LUC} uncertainty increases gradually relative to it. By the 2009–2018
 405 decade the uncertainty due to internal climate variability would account for 22% of the total E_{LUC}
 406 uncertainty. Lastly, approximately 20% of total uncertainty is from internal climate variability
 407 uncertainty for S_{OCEAN} .

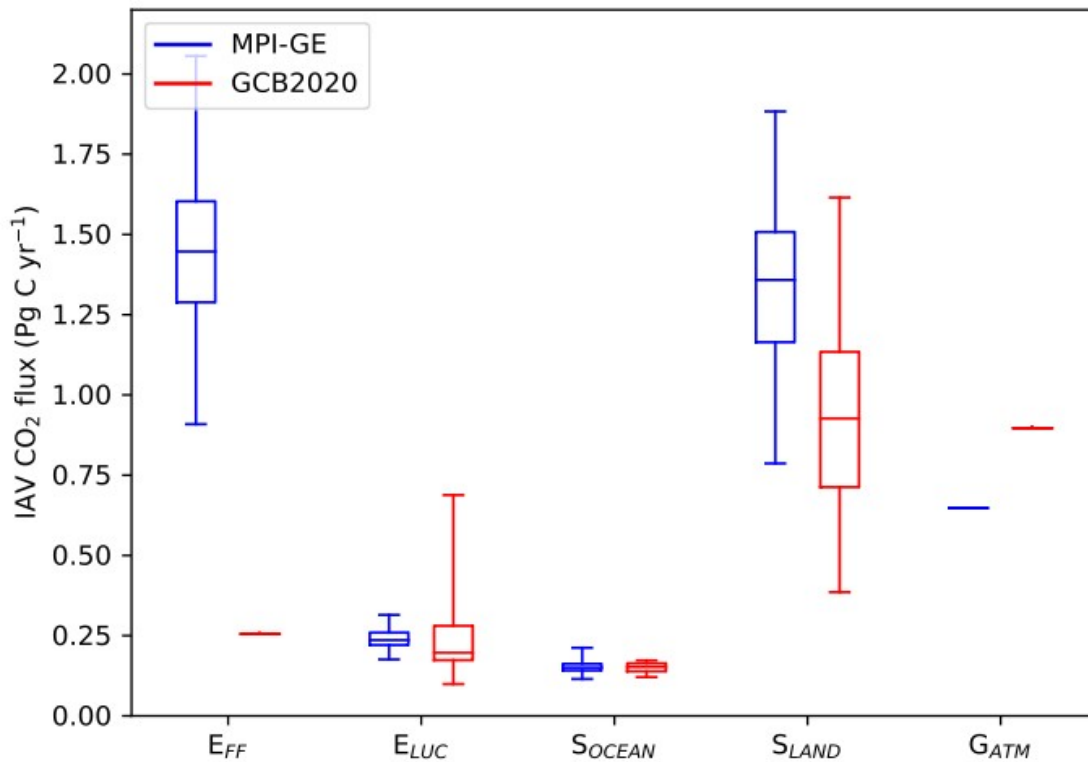


409 **Figure 6.** Centered standard deviation of carbon flux from the multi-model GCB2020 (solid
 410 lines) and ensemble standard deviation from the MPI-GE (dashed lines). The relative
 411 contribution of internal climate variability uncertainty is marked in red (dot-dashed lines
 412 corresponding to the right-hand axis). The color coding is the same as that used in Figures 2–5.

413 3.2.4 Interannual variability

414 The ability of individual ensemble members to capture the IAV (in the base period 1961–1990)
 415 for each term compared to the GCB2020 IAVs is shown in Figure 7. The ranges of the IAVs
 416 generally have good overlap for the E_{LUC} and S_{OCEAN} budget terms. This means that individual
 417 MPI-GE members can simulate a plausible range of IAV values that are not significantly
 418 different from the published values from the GCB2020. S_{LAND} , however, shows some IAV bias in
 419 the MPI-ESM compared to other models in the GCB2020. IAV in MPI-GE S_{LAND} tends to be on
 420 average 0.4 Pg C yr^{-1} larger than other models. A higher IAV may contribute to the large
 421 ensemble spread in the MPI-GE for S_{LAND} (compare to Figure 5). There are large differences
 422 between MPI-GE and GCB2020 for E_{FF} , and G_{ATM} (Figure 7). Evaluation of G_{ATM} is difficult
 423 because there is no associated uncertainty range; the GCB2020 only has one potential realization
 424 of past emissions and observed CO_2 concentration, and the MPI-GE atmospheric CO_2
 425 concentrations are prescribed. The observationally-based GCB2020 uncertainties are only 0.02

426 Pg C yr⁻¹ for G_{ATM} and at most 0.5 Pg C yr⁻¹ for residual E_{FF} and if we use these values as a range
 427 on top of the GCB2020 IAV, MPI-GE is still outside these ranges.



428

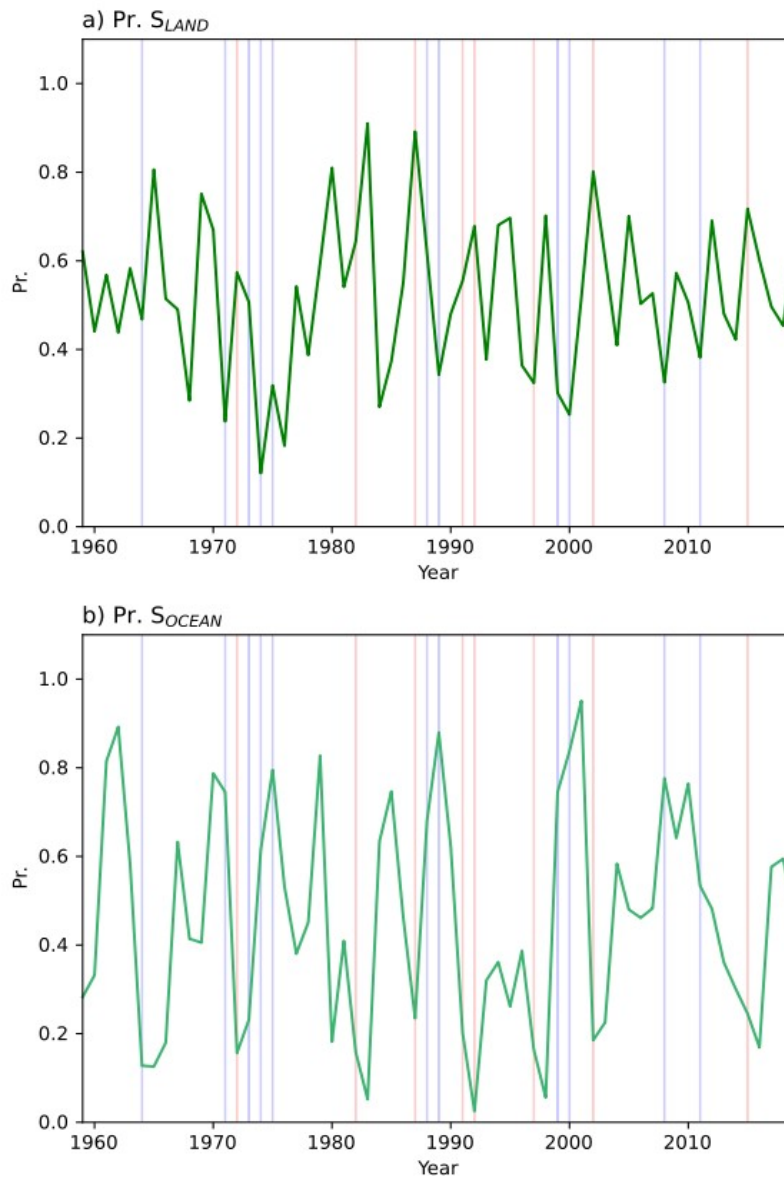
429 **Figure 7.** Box and whisker plots of interannual variability (IAV) calculated as the standard
 430 deviation over the base period 1961–1990 for the MPI-GE (blue) and the GCB2020 (red). The
 431 ranges shown here are derived from the ensemble members for MPI-GE, and from multiple
 432 model simulations for the GCB2020. The boxes mark the median and inter-quartile range, and
 433 the whiskers mark the full range of values.

434 3.3 The relationship of historical probabilities to ENSO

435 To investigate a potential source of the IAV and uncertainty from internal climate variability, we
 436 examine here the exceedance probabilities and the relationship to ENSO. Figure 8 shows the
 437 probability of the magnitude of the past carbon fluxes in GCB2020 with respect to the
 438 distribution of the MPI-GE. Higher values indicate years where the carbon flux for the respective
 439 sink was unusually small compared to the MPI-GE distribution and thus were more likely to be
 440 exceeded under more favorable climate conditions. S_{LAND} and S_{OCEAN} have large annual variations
 441 in exceedance probability. For example, since 1960 there were three years where the historical
 442 S_{LAND} was so high, related to La Niña, that it had a chance of less than 20% to be exceeded and
 443 five years with S_{LAND} so low that it had a chance of more than 80% to be exceeded (Figure 8 a).
 444 This highlights the importance of using a large ensemble to capture the high variability in S_{LAND}
 445 (see Section 4.5). The cause of these year-to-year variations may come from a variety of internal
 446 climate variability modes. To investigate potential drivers, Figure 9 shows that there are

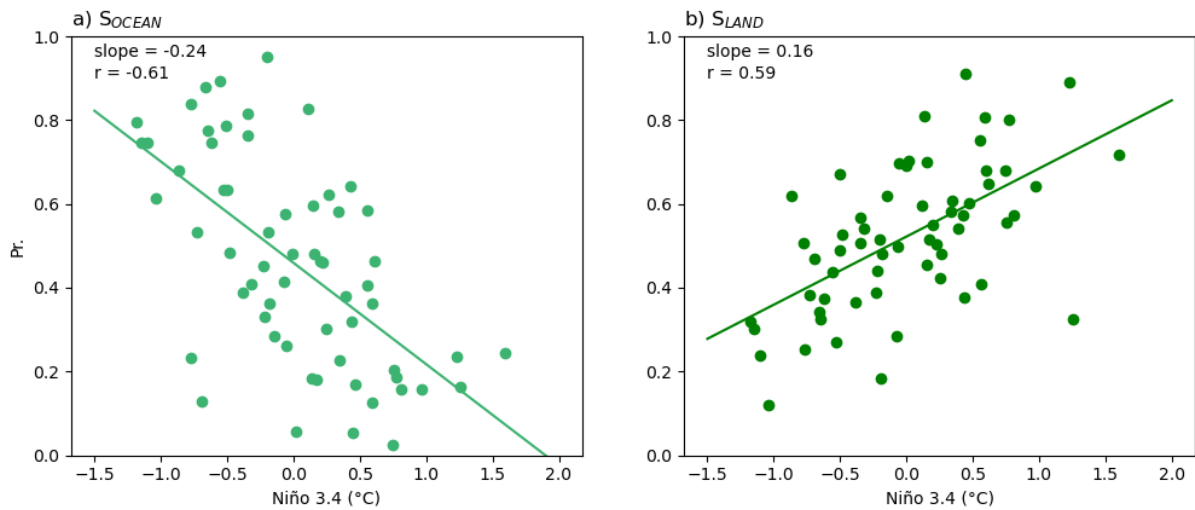
447 significant correlations between the Niño 3.4 index and S_{OCEAN} or S_{LAND} exceedance probability of
 448 -0.61 and 0.56 respectively (see also Supplementary Text and Figure S2).

449



450 **Figure 8.** Probability of exceedance that the MPI-GE carbon fluxes are greater than the historical
 451 GCB2020 mean. Lower values indicate years where the carbon flux to the respective sink was
 452 *unusually* high compared to the MPI-GE *distribution* (*vice versa* for large values). The vertical
 453 lines mark El Niño (red) and La Niña (blue) years where Niño 3.4 index is greater than 1
 454 standard deviation from the mean.

455



457 **Figure 9.** Regression and correlation analysis between Niño 3.4 index and the probability of
 458 exceedance for carbon fluxes a) S_{OCEAN} and b) S_{LAND} . The units of the slope are in $^{\circ}\text{C}^{-1}$.

459 4 Discussion

460 In summary, S_{LAND} has the largest uncertainty, which emphasizes the dominant role of internal
 461 climate variability on the land sink (Figure 3 d). This uncertainty gradually increases over time to
 462 approximately $\pm 1.5 \text{ Pg C yr}^{-1}$. While the global S_{LAND} flux and CO_2 concentration increases until
 463 the middle of the 21st century (Figure 2), afterwards its signal-to-noise ratio of the mean flux
 464 nevertheless decreases (Figure 4 b). The internal climate variability uncertainty in E_{LUC} is
 465 relatively smaller at approximately $\pm 0.2 \text{ Pg C yr}^{-1}$ (Figure 3 b). However, the trend in E_{LUC}
 466 variability is likely due to a combination of sensitivity to initial conditions and the time delay
 467 associated with legacy land-use change emissions. The S_{OCEAN} variations from internal climate
 468 variability are similarly small as those in E_{LUC} but show almost no trend (Figure 3 c). The S_{LAND}
 469 internal climate variability accounts for about 70% of the total uncertainty that results from both
 470 internal variability and uncertainties from models and observations (Figure 6 d), much more than
 471 for E_{LUC} (approximately 22%) and S_{OCEAN} (approximately 19%). The standard deviations of the
 472 MPI-GE compare well with the uncertainty ranges of the GCB2020 for most budget terms: with
 473 respect to the ensemble standard deviation against multi-model standard deviations (usually at
 474 least an overlap, Figure 5), and with respect to individual ensemble IAV against individual
 475 model IAV in the GCB2020 (Figure 7). Finally, we show that the effect of internal climate
 476 variability on the historically observed exceedance probabilities of carbon fluxes to the land and
 477 ocean have significant but moderate correlations to ENSO (Figure 9).

478 4.1 Differences between MPI-GE and GCB2020

479 One of the most striking differences between the MPI-GE and the GCB2020 estimates is in E_{LUC} ,
 480 where the forced ensemble mean signal from land-use change in the RCP4.5 scenario differs
 481 from the observed LUH2 data in the last historical decade. The MPI-GE E_{LUC} transitions to a net
 482 sink at around 2020, while the forcing used in GCB2020 estimates sustained E_{LUC} until this
 483 period (Friedlingstein et al. 2020, Bastos et al. 2020). Given that the variance of E_{LUC} ensemble

484 members is quite small compared to the forced mean response, the disparity between the RCP4.5
 485 land-use change and the GCB2020 becomes evident. The RCP4.5 scenario is characterized by a
 486 high CO₂ price that encourages investment into agricultural intensification rather than expansion.
 487 Consequently, re-/afforestation would occur following widespread abandonment of agricultural
 488 lands and substantial deforestation reduction since 2007 (Thomson et al. 2011). Despite the
 489 process of forest regrowth (such as that in North America and Europe; Doelman et al. 2020)
 490 being slow, the MPI-GE reduction in E_{LUC} associated with stopping deforestation globally (in
 491 particular the Amazon and other tropical regions) is quick and modeling studies simulate
 492 substantial carbon uptake by re-/afforestation and reduced deforestation. For example, Sonntag et
 493 al. (2016) estimate an uptake of about 200 Pg C over the 21st century with RCP4.5 land-use
 494 change in an RCP8.5 climate compared to unmitigated deforestation. However, the trajectory of
 495 RCP4.5 land-use change has not been followed until now, and so the land-use-related mitigation
 496 potential remains untapped. This explains the large divergence of our results from the GCB2020
 497 estimates for the last 15 years.

498 There are also considerable differences in the “compatible” residual E_{FF} in the MPI-GE
 499 compared to the GCB2020 values. If we assume the GCB2020 estimate to be the closest estimate
 500 to the mean in reality, then the MPI-GE first underestimates the E_{FF} then overestimates it. The
 501 discrepancy may arise due to the closure of the carbon balance and the consequent effect that
 502 S_{LAND} has on the compatible emissions. On the other hand, the GCB2020 has an imbalance term
 503 that includes carbon fluxes that remain unaccounted for. This term would include errors
 504 introduced by the calculation of budget terms independently (e.g. model bias errors in E_{LUC} and
 505 S_{LAND} , e.g. Dai and Fung, 1993), errors from incomplete coverage of observations, and minor
 506 terms that are not included in the budget decomposition. For these reasons, we would not expect
 507 the MPI-GE to accurately reproduce E_{FF} .

508 Lastly, another approach to evaluating the MPI-GE against the GCB2020 is to verify that
 509 there are no trends in the budget imbalance relative to the GCB2020. If the compatible residual
 510 E_{FF} in the MPI-GE budget is replaced with the CMIP5 E_{FF} values (Figure 2b), a budget
 511 imbalance term (B_{IM}) can be calculated that is the residual carbon flux that is not accounted for
 512 under each ensemble member’s climate state. This simulated B_{IM} term (Figure S1 f) derived from
 513 the MPI-GE is largely consistent with the B_{IM} from the GCB2020 and shows no significant long-
 514 term trends over the analysis period. Both MPI-GE and GCB2020 show as a positive B_{IM} around
 515 the 1950s and again more briefly in the 1990s (suggesting either an overestimate in the emissions
 516 or underestimate in the sinks). While Friedlingstein et al. (2020) could not directly attribute a
 517 cause to the B_{IM} , they suggest that its variations originate mostly from S_{LAND} and S_{OCEAN} .
 518 Specifically, they suggest that it could originate from internal variability which models cannot
 519 capture with a single realization. However, the multiple realizations in the MPI-GE B_{IM} range
 520 also show positive values in the 1950’s, which suggests that it is more likely from common
 521 deficiencies in model physics, resolution, or forcing data. In particular, the land-use forcing
 522 could explain the 1950s B_{IM} , as the LUH2 forcing creates large emissions in the 1950s (e.g.,
 523 Hansis et al. 2015) not captured by datasets based on other land-use forcing such as FAO
 524 (Houghton and Nassikas 2017).

525 4.2 Allowable emissions under RCP4.5

526 The standard deviations in the MPI-GE (Figure 2) are derived either directly from the ensembles
 527 or are inferred from other budget terms, and therefore they should be interpreted with care. The

528 standard deviation of residual E_{FF} is mostly derived from S_{LAND} due to its calculation as a
529 residual. In this case, the ranges here are merely a range of emissions that are compatible with
530 the likely range of climate states, and the corresponding strengths of the ocean and land sinks.
531 Therefore, the residual E_{FF} uncertainty estimates from MPI-GE should not be interpreted as
532 variations in fossil fuel emissions due to internal climate variability-related global demand.

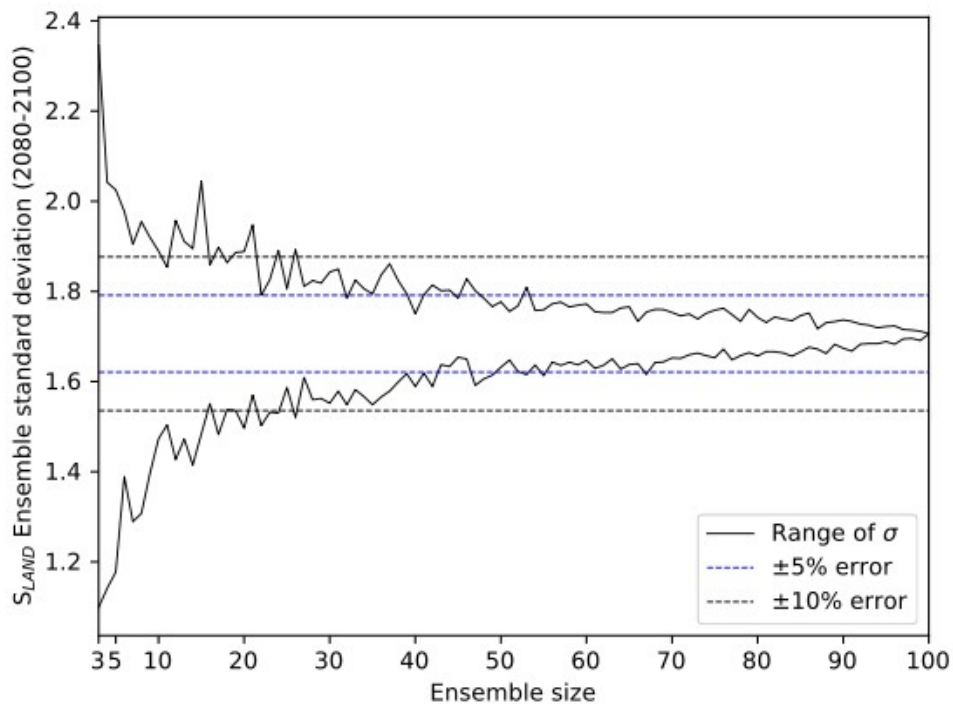
533 The net sinks and the corresponding compatible residual E_{FF} range are still useful when
534 deciding what the allowable future emissions may be. They indicate the allowable emissions
535 (accounting for internal climate variability) if appropriate policies are implemented to
536 successfully mitigate climate change in a manner that is consistent with the RCP4.5 scenario.
537 Therefore, the maximum and minimum ensemble ranges of 9–18 Pg C yr⁻¹ in residual E_{FF} at 2050
538 denote allowable emissions under this scenario (2019 was 9.95 Pg C yr⁻¹ as per the GCB2020).
539 In Fig 2 the ± 1 standard deviation range of the ensemble is shown instead. In the comparison it is
540 clear that extreme outliers occur mainly at the maximum end. These maximum values may occur
541 before fossil emissions have to drop steeply in the MPI-GE and level off at around 5 Pg C yr⁻¹ if
542 the 3°C target is to be met by 2100. This evolution matches well the fossil emissions estimates
543 from GCAM (Thomson et al. 2011) but allows some higher peak emissions than the Integrated
544 Assessment Model assumed, suggesting smaller assumed sinks and slightly larger E_{LUC} in the
545 simplified carbon cycle of this assessment model (see Figure 2 to compare to E_{FF} and E_{LUC} from
546 GCAM).

547 As highlighted by Mankin et al. (2020), decision makers need to be provided the full
548 range of possible outcomes in order to make appropriate decisions. For example, policy
549 decisions based only on the most likely outcome may lead to a blowout of greenhouse gas
550 inventory targets, particularly if S_{LAND} performs poorly within a given 5-year accounting period
551 of the Paris Agreement's Global Stocktake (UNFCCC, 2015 and 2017). On the other hand,
552 caution should be taken when considering the efficacy of past decision making because internal
553 variability uncertainties can potentially obfuscate emission reduction efforts such as
554 re-/afforestation.

555 4.3 Trends in uncertainty

556 The increase in standard deviation in the ensemble members for S_{LAND} may be due to an increase
557 in the variability in the climate state as is expected under a warming climate. For example,
558 Maher et al. (2019) find an increase in the global mean precipitation variability in the MPI-GE
559 1% CO₂ scenario. The trend in S_{LAND} internal variability can also potentially arise from the
560 increase in the magnitude of fossil emissions, which is initially forced in the MPI-GE as the
561 prescribed atmospheric CO₂ concentration. Larger emissions would result in higher atmospheric
562 CO₂ concentrations and increased potential carbon uptake by vegetation via so-called CO₂
563 fertilization (Walker et al. 2021). This combined with the effect of unfavorable climatic
564 conditions (i.e. heat and drought stress) on the carbon uptake by plants acting on an increased
565 carbon stock, results in a larger variance depending on the climate conditions. The increasing
566 internal variability makes it more likely that S_{LAND} becomes near-neutral by the end of the
567 century compared to the start of the historical period (Figure S1 d). This contrasts somewhat with
568 S_{OCEAN} , which has a relatively lower variance and does not have a trend in the historical or future
569 periods under the RCP4.5 scenario (a similar standard deviation is found by Li and Ilyina 2018).
570 However, under higher emissions scenarios S_{OCEAN} has been shown to also have increasing trends
571 in CO₂ flux standard deviation (see Figure 1 of Maher et al. 2019).

572 The trend in E_{LUC} may arise for several reasons. Firstly, the legacy effects of land-use
 573 change (mostly from wood harvest) take time to manifest. The anthropogenic pools in which
 574 CBALONE stores deforested biomass decay to the atmosphere at time scales of 1–100 years.
 575 The variance of the ensemble members therefore not only depends on the climate variability of
 576 the current year but also on that of preceding years. Consequently, it would take at least 100
 577 years for the full variance due to land-use change to manifest. Similarly, the carbon pool of
 578 woody, slowly-decomposing litter left on site after clearing or harvesting will build up over time
 579 as land-use transitions occur. Thus, more litter is available to react to the climate-dependent
 580 microbial decomposition. Note that while the study of Yue et al. (2020) included this effect in
 581 their assessment of the contribution of land-use to the interannual variability of the land carbon
 582 pools, their high IAV of E_{LUC} (30–45% of net land exchange IAV, compared to 15% in this
 583 study) also originates from attributing part of S_{LAND} (the part on managed land) to E_{LUC} . Internal
 584 variability alone, our study shows, is about $0.25 \text{ Pg C yr}^{-1}$ standard deviation for E_{LUC} in recent
 585 decades (Figure 3) or 20% of the total uncertainty (model plus internal; Figure 6). IAV of E_{LUC} in
 586 the MPI-GE is only slightly larger than in the GCB2020 (Figure 7), indicating that the main
 587 driver is not internal climate variability, but land-use forcing.
 588



589 **Figure 10.** Range of ensemble standard deviation (2080–2100) as a function of sample size from
 590 30 sub-samples for S_{LAND} .

591 While the data analyzed in this study is annual and much of the analysis concerns
 592 interannual variations, we conducted simulations for several centuries, and therefore the longer
 593 time scale variations must also be considered. There are centennial-scale internal variations in
 594 the land carbon content in JSBACH3 and CBALONE (see Figure 2 in Schneck et al. 2013)

595 which could influence trends and variability of S_{LAND} and E_{LUC} for simulations that run for several
596 hundred years. These variations have a periodicity of ~ 250 years and consist of a change in the
597 total land carbon content of ~ 8 Pg C. This corresponds to an average land carbon flux of 0.03 Pg
598 C yr^{-1} or roughly 2% of the MPI-GE S_{LAND} standard deviation. Schneck et al. (2013) suggest that
599 these long-duration variations in land carbon content are linked to variations in anthropogenic
600 land cover changes, and the modulation of soil respiration by long-term changes in temperature
601 from volcanism and solar forcing. Since the duration of the MPI-GE and CBALONE simulation
602 in this study is 250 years, it is possible that these long-term variations may affect the estimates of
603 internal climate variability uncertainty in S_{LAND} .

604 4.4 ENSO as a potential source of variability

605 ENSO is positively correlated with S_{LAND} exceedance probabilities and negatively correlated with
606 S_{OCEAN} exceedance probabilities, which is consistent with how ENSO affects CO_2 fluxes to the
607 land surface and ocean. During La Niña, cool and moist mean global conditions tend to
608 encourage vegetative productivity on land and increase land carbon storage, while El Niño
609 drought conditions put widespread stress on ecosystems and suppress productivity (Gonsamo et
610 al. 2016; Jones et al. 2001). Meanwhile, over the ocean, stronger pacific equatorial up-welling
611 during La Niña brings dissolved inorganic carbon-rich subsurface water to the surface, thereby
612 favoring CO_2 out-gassing and reducing net CO_2 uptake (Jones et al. 2001; Feely et al. 1999). The
613 cooler sea surface temperatures during La Niña events can increase the dissolution of CO_2 and
614 can reduce CO_2 outgassing, but this is a smaller term relative to the up-welling-induced CO_2
615 outgassing. This could explain the diverging response of S_{OCEAN} to ENSO compared to that of
616 S_{LAND} . The moderate correlation suggests that while ENSO may have a considerable impact on
617 interannual variations in CO_2 fluxes, it is very likely that other climate modes and internal
618 dynamics are also important. No significant correlations with other climate modes could be
619 found at the global scale, however the impacts of climate modes on regional budgets may be
620 considerable.

621 4.5 Importance of ensemble size

622 Lastly, it is important to discuss the effect of ensemble size on the results and whether or not
623 using 100 members is enough or more than necessary. A framework to assess this is
624 demonstrated in Milinski et al. (2020). In accordance with this framework, our goal is to quantify
625 variability using the metric of ensemble standard deviation, to within 5% accuracy of the full 100
626 member variance. We estimate standard deviation using 30 iterations of subsample sizes from 3–
627 100 members without replacement. Figure 10 suggests that at least 40 ensemble members are
628 required to capture the standard deviation of S_{LAND} to within $\pm 5\%$ accuracy. Since S_{LAND} has the
629 largest standard deviation of all budget terms, the accuracy of a sub-sample of the carbon budget
630 decomposition would depend on this term. The other budget terms (Figure S5) do not display
631 variations as large as S_{LAND} and therefore 40 members are sufficient for those terms. Whether this
632 result is representative of other models that simulate internal variability through ensemble
633 simulations depends on the budget terms. In the absence of extensive multi-model large
634 ensemble projects that provide the full suite of budget terms, including the split into S_{LAND} and
635 E_{LUC} , we evaluated this based on the IAV in the models participating in the GCB2020
636 simulations that are forced with observed climate (Figure 7). A key assumption is that MPI-GE is
637 capable of accurately representing IAV, and the fact that MPI-GE slightly overestimates S_{LAND}

638 IAV by 0.4 Pg C yr^{-1} compared to other models in the GCB2020 suggests that the minimum 40
639 ensemble members required here may be a conservative estimate.

640 5 Conclusion

641 In this study, we use a large ensemble of single-model simulations from the Max Planck Institute
642 Grand Ensemble and a sub-component of JSBACH3 (called CBALONE) to decompose the
643 global anthropogenic carbon budget into fossil and land-use change emissions, atmospheric
644 growth, and natural land and ocean sinks. Through its 100 ensemble members, the MPI-GE
645 captures the uncertainties associated with internal climate variability, which we compare to the
646 2020 global carbon budget's uncertainty and interannual variability, and calculate exceedance
647 probabilities of the past carbon fluxes with respect to a full range of climate variability states.
648 We estimate about 40 ensemble members are required to capture internal variability in S_{LAND} and
649 thus all budget components. Contrary to S_{LAND} , to reduce uncertainty in S_{OCEAN} and E_{LUC}
650 estimates, we must prioritize reducing observational error and model spread rather than capturing
651 internal variability. Despite its high internal variability, S_{LAND} (or S_{OCEAN}) is likely not the reason
652 behind the high budget imbalance found in previous studies for the 1950s, which suggests
653 common model deficiencies or biases in the land-use forcing.

654 We also present a novel estimate of the uncertainty in land-use change emissions
655 associated with internal climate variability at approximately $\pm 0.2 \text{ Pg C yr}^{-1}$, which we estimate
656 would account for about 20% of the total (internal and multi-model) land-use change emissions
657 uncertainties. Land-use change emissions thus contribute little to interannual variability of the
658 annual carbon budget and are driven rather by land-use forcing than by climate variability.

659 We investigate future changes in the global carbon budget under RCP4.5 and demonstrate
660 upper and lower bounds on the allowable future CO_2 emissions depending on climate variations.
661 The RCP4.5 scenario exemplifies a future where climate policies are implemented to limit
662 warming to less than 3°C over present-day conditions. Our study largely confirms that the
663 allowable emissions under the assumptions of the socioeconomic model GCAM are compatible
664 with RCP4.5, though slightly higher emissions of up to 13 Pg C yr^{-1} on average would be
665 allowed in the MPI-ESM. The minimum of the full ensemble range is 9 Pg C yr^{-1} and would be
666 the lower risk limit to ensure we stay below 3°C warming for all possible climate states, while
667 the maximum of 18 Pg C yr^{-1} would be the higher risk limit for the climate states leading to
668 stronger land CO_2 uptake. Our results suggest that internal variability of the natural land sink
669 increases over the 21st century, which puts the steady persistence of carbon removal by land
670 ecosystems at risk. We also show that even when accounting for random variations in climate
671 and natural sinks, the emissions in recent decades for land-use change—characterized by
672 continuing global deforestation—are dangerously inconsistent with the RCP4.5 goals and further
673 erode our ability to successfully mitigate future warming.

674 Acknowledgments

675 The authors would like to acknowledge the generous help and comments from the Max Planck
676 Institute Grand Ensemble working group. We also thank the German Climate Computing Centre
677 (DKRZ), for providing computational resources. CMIP5 emissions data are available from RCP
678 Database <http://www.iiasa.ac.at/web-apps/tnt/RcpDb> and the GCP Global Carbon Budgets data
679 are available from <https://www.globalcarbonproject.org/carbonbudget/archive.htm>. H.L. was

680 supported by the European Union's Horizon 2020 research and innovation program under grant
681 agreement no. 821003 (4C).

682

684 **References**

- 685 Andres, R. J., et al. (2012), A synthesis of carbon dioxide emissions from fossil-fuel combustion.
686 *Biogeosciences*, **9**, 1845–1871, doi:[10.5194/bg-9-1845-2012](https://doi.org/10.5194/bg-9-1845-2012).
- 687 Ballantyne, A. P., C. B. Alden, J. B. Miller, P. P. Tans, and W. C. White, (2012), Increase in
688 observed net carbon dioxide uptake by land and oceans during the past 50 years. *Nature*,
689 **488**, 70–72, doi:[10.1038/nature11299](https://doi.org/10.1038/nature11299).
- 690 Bastos, A., S. W. Running, C. Gouveia, and R. M. Trigo (2013), The global NPP dependence on
691 ENSO: La Niña and the extraordinary year of 2011: GLOBAL NPP AND ENSO: THE
692 2011 LA NIÑA. *Journal of Geophysical Research: Biogeosciences*, **118**, 1247–1255,
693 doi:[10.1002/jgrg.20100](https://doi.org/10.1002/jgrg.20100).
- 694 Bastos, A., et al. (2018), Impact of the 2015/2016 El Niño on the terrestrial carbon cycle
695 constrained by bottom-up and top-down approaches. *Philosophical Transactions of the*
696 *Royal Society B Biological Sciences*, **373**, 20170304, doi:[10.1098/rstb.2017.0304](https://doi.org/10.1098/rstb.2017.0304).
- 697 Canadell, J. G. *et al.* (2007), Contributions to accelerating atmospheric CO₂ growth from
698 economic activity, carbon intensity, and efficiency of natural sinks. *Proceedings of the*
699 *National Academy of Sciences* **104**, 18866–18870, doi:[10.1073/pnas.0702737104](https://doi.org/10.1073/pnas.0702737104).
- 700 Climate Prediction Center (2017), *Monthly Atmospheric SST Indices*,
701 <https://www.cpc.ncep.noaa.gov/data/indices/>.
- 702 Conway, T. J., P. P. Tans, L. S. Waterman, K. W. Thoning, D. R. Kitzis, K. A. Masarie, and N.
703 Zhang, 1994: Evidence for interannual variability of the carbon cycle from the National
704 Oceanic and Atmospheric Administration/Climate Monitoring and Diagnostics
705 Laboratory Global Air Sampling Network. *Journal Geophysical Resesearch Atmospheres*,
706 **99**, 22831–22855, doi:[10.1029/94JD01951](https://doi.org/10.1029/94JD01951).
- 707 Dai, A. and Fung, I. Y. (1993), Can climate variability contribute to the ‘Missing’ CO₂ sink?
708 *Global Biogeochemical Cycles* **7**, 599–609, doi:[10.1029/93GB01165](https://doi.org/10.1029/93GB01165).
- 709 Dannenberg, M. P., C. Song, T. Hwang, and E. K. Wise (2015), Empirical evidence of El Niño–
710 Southern Oscillation influence on land surface phenology and productivity in the western
711 United States. *Remote Sensing Environment*, **159**, 167–180,
712 doi:[10.1016/j.rse.2014.11.026](https://doi.org/10.1016/j.rse.2014.11.026).
- 713 Deser, C., Phillips, A., Bourdette, V. and Teng, H., (2012), Uncertainty in climate change
714 projections: the role of internal variability. *Climate Dynamics* **38**, 527–546,
715 doi:[10.1007/s00382-010-0977-x](https://doi.org/10.1007/s00382-010-0977-x).
- 716 Dlugokencky, E., and P. Tans (2018), *Trends in atmospheric carbon dioxide*, National Oceanic
717 & Atmospheric Administration, Earth System Research Laboratory (NOAA/ESRL).
- 718 Doelman, J. C., et al. (2020), Afforestation for climate change mitigation: Potentials, risks and
719 trade-offs. *Global Change Biology*, **26**, 1576–1591, doi:[10.1111/gcb.14887](https://doi.org/10.1111/gcb.14887) .

- 720 Feely, R. A., R. Wanninkhof, T. Takahashi, and P. Tans (1999), Influence of El Niño on the
721 equatorial Pacific contribution to atmospheric CO₂ accumulation. *Nature* **398**, 597–601,
722 doi:[10.1038/19273](https://doi.org/10.1038/19273).
- 723 Friedlingstein, P., et al. (2019), Global Carbon Budget 2019. *Earth System Science Data*, **11**,
724 1783–1838, doi:[10.5194/essd-11-1783-2019](https://doi.org/10.5194/essd-11-1783-2019).
- 725 Giorgetta, M. A., et al. (2013), Climate and carbon cycle changes from 1850 to 2100 in MPI-
726 ESM simulations for the Coupled Model Intercomparison Project phase 5. *Journal of*
727 *Advances in Modeling Earth Systems*, **5**, 572–597, doi:[10.1002/jame.20038](https://doi.org/10.1002/jame.20038).
- 728 Goll, D. S. et al. (2015), Strong dependence of CO₂ emissions from anthropogenic land cover
729 change on initial land cover and soil carbon parametrization. *Global Biogeochemical*
730 *Cycles*, **29**, 1511–1523, doi:[10.1002/2014GB004988](https://doi.org/10.1002/2014GB004988).
- 731 Gonsamo, A., J. M. Chen, and D. Lombardozzi (2016), Global vegetation productivity response
732 to climatic oscillations during the satellite era. *Global Change Biology*, **22**, 3414–3426,
733 <https://doi.org/10.1111/gcb.13258>.
- 734 Hansis, E., S. J. Davis, and J. Pongratz (2015), Relevance of methodological choices for
735 accounting of land use change carbon fluxes. *Global Biogeochemical Cycles*, **29**, 1230–
736 1246, doi:[10.1002/2014GB004997](https://doi.org/10.1002/2014GB004997).
- 737 Houghton, R. A., and A. A. Nassikas (2017), Global and regional fluxes of carbon from land use
738 and land cover change 1850-2015: Carbon Emissions From Land Use. *Global*
739 *Biogeochemical Cycles*, **31**, 456–472, doi:[10.1002/2016GB005546](https://doi.org/10.1002/2016GB005546).
- 740 Huang, B., et al. (2017), Extended Reconstructed Sea Surface Temperature, Version 5
741 (ERSSTv5): Upgrades, Validations, and Intercomparisons. *Journal of Climate*, **30**, 8179–
742 8205, doi:[10.1175/JCLI-D-16-0836](https://doi.org/10.1175/JCLI-D-16-0836).
- 743 Hurtt, G. C., et al. (2011), Harmonization of land-use scenarios for the period 1500-2100: 600
744 years of global gridded annual land-use transitions, wood harvest, and resulting
745 secondary lands. *Climate Change*, **109**, 117–161, doi:[10.1007/s10584-011-0153-2](https://doi.org/10.1007/s10584-011-0153-2).
- 746 Ilyina, T., K. D. Six, J. Segschneider, E. Maier-Reimer, H. Li, and I. Núñez-Riboni (2013),
747 Global ocean biogeochemistry model HAMOCC: Model architecture and performance as
748 component of the MPI-Earth system model in different CMIP5 experimental realizations:
749 The Model Hamoccc within Mpi-Esm in C mip5. *Journal of Advances in Modeling Earth*
750 *Systems*, **5**, 287–315, doi:[10.1029/2012MS000178](https://doi.org/10.1029/2012MS000178).
- 751 Jones, C., et al. (2013), Twenty-First-Century Compatible CO₂ Emissions and Airborne Fraction
752 Simulated by CMIP5 Earth System Models under Four Representative Concentration
753 Pathways. *Journal of Climate*, **26**, 4398–4413, doi:[10.1175/JCLI-D-12-00554](https://doi.org/10.1175/JCLI-D-12-00554).
- 754 Jones, C. D., M. Collins, P. M. Cox, and S. A. Spall (2001), The Carbon Cycle Response to
755 ENSO: A Coupled Climate–Carbon Cycle Model Study. *Journal of Climate*, **14**, 17,
756 doi:[10.1175/1520-0442\(2001\)014<4113:TCCRTE>2.0.CO;2](https://doi.org/10.1175/1520-0442(2001)014<4113:TCCRTE>2.0.CO;2).
- 757 Kay, J. E. et al. (2015), The Community Earth System Model (CESM) Large Ensemble Project:
758 A Community Resource for Studying Climate Change in the Presence of Internal Climate
759 Variability. *Bulletin of the American Meteorological Society* **96**, 1333–1349,
760 doi:[10.1175/BAMS-D-13-00255.1](https://doi.org/10.1175/BAMS-D-13-00255.1).

- 761 Lawrence, P. J. et al. (2012), Simulating the Biogeochemical and Biogeophysical Impacts of
762 Transient Land Cover Change and Wood Harvest in the Community Climate System
763 Model (CCSM4) from 1850 to 2100. *J. Climate*, 25, 3071–3095, doi:10.1175/JCLI-D-11-
764 00256.1.
- 765 Le Quéré, C., et al. (2013), The global carbon budget 1959–2011. *Earth System Science Data*, 5,
766 165–185, doi:[10.5194/essd-5-165-2013](https://doi.org/10.5194/essd-5-165-2013).
- 767 —, et al. (2018a), Global Carbon Budget 2017. *Earth System Science Data*, 10, 405–448,
768 doi:[10.5194/essd-10-405-2018](https://doi.org/10.5194/essd-10-405-2018).
- 769 —, et al. (2018b), Global Carbon Budget 2018. *Earth System Science Data*, 10, 2141–2194,
770 doi:[10.5194/essd-10-2141-2018](https://doi.org/10.5194/essd-10-2141-2018).
- 771 Li, H., and T. Ilyina (2018), Current and Future Decadal Trends in the Oceanic Carbon Uptake
772 Are Dominated by Internal Variability. *Geophysical Research Letters*, 45, 916–925,
773 doi:[10.1002/2017GL075370](https://doi.org/10.1002/2017GL075370).
- 774 Maher, N., et al. (2019), The Max Planck Institute Grand Ensemble: Enabling the Exploration of
775 Climate System Variability. *Journal of Advances in Modeling Earth Systems*, 11, 2050–
776 2069, doi:[10.1029/2019MS001639](https://doi.org/10.1029/2019MS001639).
- 777 Mankin, J. S., F. Lehner, S. Coats, and K. A. McKinnon (2020), The Value of Initial Condition
778 Large Ensembles to Robust Adaptation Decision-Making. *Earth's Future* 8,
779 doi:[10.1029/2020EF001610](https://doi.org/10.1029/2020EF001610).
- 780 Marsland, S. J., H. Haak, J. H. Jungclaus, M. Latif, and F. Röske (2003), The Max-Planck-
781 Institute global ocean/sea ice model with orthogonal curvilinear coordinates. *Ocean*
782 *Modelling*, 5, 91–127, doi:[10.1016/S1463-5003\(02\)00015-X](https://doi.org/10.1016/S1463-5003(02)00015-X).
- 783 Meinshausen, M., et al. (2017), Historical greenhouse gas concentrations for climate modelling
784 (CMIP6). *Geoscientific Model Development*, 10, 2057–2116, doi:[10.5194/gmd-10-2057-
785 2017](https://doi.org/10.5194/gmd-10-2057-2017).
- 786 Millar, R. J. et al. (2017), Emission budgets and pathways consistent with limiting warming to
787 1.5 °C. *Nature Geoscience* 10, 741–747, doi:[10.1038/ngeo3031](https://doi.org/10.1038/ngeo3031).
- 788 Milinski, S., N. Maher, and D. Olonscheck (2020), How large does a large ensemble need to be?
789 *Earth System Dynamics*, 11, 885–901, doi:[10.5194/esd-11-885-2020](https://doi.org/10.5194/esd-11-885-2020).
- 790 Pongratz, J., C. H. Reick, R. A. Houghton, and J. I. House (2014), Terminology as a key
791 uncertainty in net land use and land cover change carbon flux estimates. *Earth System*
792 *Dynamics*, 5, 177–195, doi:[10.5194/esd-5-177-2014](https://doi.org/10.5194/esd-5-177-2014).
793
- 794 Poulter, B., et al. (2014), Contribution of semi-arid ecosystems to interannual variability of the
795 global carbon cycle. *Nature*, 509, 600–603, doi:[10.1038/nature13376](https://doi.org/10.1038/nature13376).
- 796 Reick, C. H., T. Raddatz, V. Brovkin, and V. Gayler (2013), Representation of natural and
797 anthropogenic land cover change in MPI-ESM. *Journal of Advances in Modeling Earth*
798 *Systems*, 5, 459–482, doi:[10.1002/jame.20022](https://doi.org/10.1002/jame.20022).
- 799 Roeckner, E., Giorgetta, M. A., Crueger, T., Esch, M. and Pongratz, J. (2010), Historical and
800 future anthropogenic emission pathways derived from coupled climate-carbon cycle
801 simulations. *Climatic Change* 105, 91–108, doi:[10.1007/s10584-010-9886-6](https://doi.org/10.1007/s10584-010-9886-6).

- 802 Rogelj, J. *et al.* (2016), Differences between carbon budget estimates unravelled. *Nature Clim*
803 *Change* **6**, 245–252, doi:[10.1038/nclimate2868](https://doi.org/10.1038/nclimate2868).
- 804 Schneck, R., C. H. Reick, and T. Raddatz (2013) Land contribution to natural CO₂ variability on
805 time scales of centuries: Land Contribution to CO₂ Variability. *Journal of Advances in*
806 *Modeling Earth Systems*, **5**, 354–365, doi:[10.1002/jame.20029](https://doi.org/10.1002/jame.20029).
- 807 Scott, D. W. (2015), *Multivariate density estimation: theory, practice, and visualization*. John
808 Wiley & Sons.
- 809 Shapiro, S. S. and Wilk (1965), M. B. An Analysis of Variance Test for Normality (Complete
810 Samples). *Biometrika* **52**, 591–611, doi:[10.2307/2333709](https://doi.org/10.2307/2333709).
- 811 Sonntag, S., J. Pongratz, C. H. Reick, and H. Schmidt (2016), Reforestation in a high-CO₂ world
812 —Higher mitigation potential than expected, lower adaptation potential than hoped for.
813 *Geophysical Research Letters*, **43**, 6546–6553, doi:[10.1002/2016GL068824](https://doi.org/10.1002/2016GL068824).
- 814 Stevens, B., *et al.* (2013), Atmospheric component of the MPI-M Earth System Model:
815 ECHAM6: ECHAM6. *Journal of Advances in Modeling Earth Systems*, **5**, 146–172,
816 doi:[10.1002/jame.20015](https://doi.org/10.1002/jame.20015).
- 817 Suarez-Gutierrez, L., Müller, W. A., Li, C. and Marotzke, J. (2020), Hotspots of extreme heat
818 under global warming. *Climate Dynamics* **55**, 429–447, doi:[10.1007/s00382-020-05263-](https://doi.org/10.1007/s00382-020-05263-w)
819 [w](https://doi.org/10.1007/s00382-020-05263-w).
- 820 Taylor, K. E., Stouffer, R. J. and Meehl, G. A. (2012), An overview of CMIP5 and the
821 experiment design. *Bulletin of the American Meteorological Society* **93**, 485–498,
822 doi:[10.1175/BAMS-D-11-00094.1](https://doi.org/10.1175/BAMS-D-11-00094.1).
- 823 UNFCCC (2015), *Paris Agreement*, Article 14.
- 824 UNFCCC (2017), *Report of the Subsidiary Body for Scientific and Technological Advice on its*
825 *forty-fifth session, held in Marrakech from 7 to 15 November 2016*.
- 826 Thomson, A. M., *et al.* (2011), RCP4.5: A pathway for stabilization of radiative forcing by 2100.
827 *Climate Change*, **109**, 77–94, doi:[10.1007/s10584-011-0151-4](https://doi.org/10.1007/s10584-011-0151-4).
- 828 Walker, A. P. *et al.* (2021) Integrating the evidence for a terrestrial carbon sink caused by
829 increasing atmospheric CO₂. *New Phytologist* **229**, 2413–2445 (2021).
- 830 Yue, C., Ciais, P., Houghton, R. A. and Nassikas, A. A. (2020), Contribution of land use to the
831 interannual variability of the land carbon cycle. *Nature Communications* **11**, 3170,
832 doi:[10.1038/s41467-020-16953-8](https://doi.org/10.1038/s41467-020-16953-8).
- 833 Zhang, Y., M. P. Dannenberg, T. Hwang, and C. Song (2019), El Niño–Southern Oscillation-
834 Induced Variability of Terrestrial Gross Primary Production During the Satellite Era.
835 *Journal of Geophysical Research Biogeosciences*, **124**, 2419–2431,
836 doi:[10.1029/2019JG005117](https://doi.org/10.1029/2019JG005117).
- 837 Zhu, Z., S. Piao, T. Yan, P. Ciais, A. Bastos, X. Zhang, and Z. Wang (2018), The Accelerating
838 Land Carbon Sink of the 2000s May Not Be Driven Predominantly by the Warming
839 Hiatus. *Geophysical Research Letters*, **45**, 1402–1409, doi:[10.1002/2017GL075808](https://doi.org/10.1002/2017GL075808).
- 840